HAL
open science

Probing xenon atoms and ions velocity in the magnetic nozzle of a helicon plasma thruster

A E Vinci, Stéphane Mazouffre, Marco R Inchingolo, Víctor Gómez, Pablo Fajardo, Jaume Navarro-Cavallé

To cite this version:

A E Vinci, Stéphane Mazouffre, Marco R Inchingolo, Víctor Gómez, Pablo Fajardo, et al.. Probing xenon atoms and ions velocity in the magnetic nozzle of a helicon plasma thruster. 37th International Electric Propulsion Conference, Jun 2022, Boston, United States. hal-03797333

HAL Id: hal-03797333

https://hal.science/hal-03797333v1

Submitted on 4 Oct 2022

HAL is a multi-disciplinary open access archive for the deposit and dissemination of scientific research documents, whether they are published or not. The documents may come from teaching and research institutions in France or abroad, or from public or private research centers.

L'archive ouverte pluridisciplinaire **HAL**, est destinée au dépôt et à la diffusion de documents scientifiques de niveau recherche, publiés ou non, émanant des établissements d'enseignement et de recherche français ou étrangers, des laboratoires publics ou privés.

Probing xenon atoms and ions velocity in the magnetic nozzle of a helicon plasma thruster

IEPC-2022-484

Presented at the 37th International Electric Propulsion Conference
Massachusetts Institute of Technology, Cambridge, MA, USA
June 19-23, 2022

A. E. Vinci[1] and Stéphane Mazouffre[2]
Institut de Combustion, Aérothermique, Réactivité et Environnement (ICARE),
Centre National de la Recherche Scientifique (CNRS),
1C Avenue de la Recherche Scientifique, 45071 Orléans, France

Marco R. Inchingolo[3], Víctor Gómez[4], Pablo Fajardo[5] and Jaume Navarro-Cavallé[6]
Equipo de Propulsión Espacial y Plasmas, Universidad Carlos III de Madrid,
Avenida de la Universidad 30, 28911 Leganés, Spain

The dynamics of atoms and ions expanding in the magnetic nozzle of a Helicon plasma thruster is experimentally studied by means of near-infrared laser-induced fluorescence spectroscopy and a retarding potential analyzer. The two techniques are compared in measuring Xe and Kr ion velocity for different thruster working parameters. Fluorescence spectra are recorded for several operating conditions inside and outside the thruster discharge chamber. In the near-field plume, the relatively intense magnetic field induces the Zeeman effect on the probed optical transitions. Hence, modeling of the atomic lineshapes is addressed to accurately compute the Doppler shift and infer the velocity. The first direct measurements of the neutral flow in a magnetic nozzle reveal that atoms are accelerated to supersonic velocities downstream the thruster exit. The ions acceleration region extends several centimeters downstream the exit plane. Larger axial ion speeds are attained when the thruster operates at lower mass flow rates and higher levels of input power.

I. Introduction

An increasing portion of small spacecrafts currently requires in-space maneuvering capabilities [1]. As a result, research on alternative electric propulsion technologies, e.g. electrodeless plasma thrusters among others, is an active area in the electric propulsion field [2–11]. Most of the investigated types of electrodeless devices integrate a magnetic nozzle (MN) to increase the momentum of the ejected ions thus to enhance the attained performance. A series of paramount advantages might derive from the use of electrodeless plasma thrusters with respect to the well consolidated systems, such as Gridded Ion thrusters and Hall thrusters. Perhaps the foremost attractive is that any electrodeless discharge is intrinsically current-free on the full scale, therefore no neutralizer is required. Thus, chemical compatibility of the thruster constituents does not represent a limiting factor for the exploitation of virtually any alternative propellant.

The Helicon plasma thruster (HPT) exemplifies one of the investigated electrodeless systems. In general terms, it comprises *i*) a dielectric chamber as the plasma discharge region, *ii*) a radio-frequency (rf) antenna as the source of the input power and *iii*) an applied magnetic field having two roles: *a*) to reduce the plasma-wall interaction and enhance the plasma-wave coupling efficiency within the source, *b*) to shape a divergent MN in the external region, which is

[1]PhD Student, ICARE - CNRS, alfio.vinci@cnrs-orleans.fr
[2]Research Director, Head of the Electric Propulsion team, ICARE - CNRS, stephane.mazouffre@cnrs-orleans.fr
[3]PhD Student, UC3M, minching@pa.uc3m.es
[4]PhD Student, UC3M, victor.g.garcia@alumnos.uc3m.es
[5]Associate Professor, UC3M, Aerospace Engineering Department, pablo.fajardo@uc3m.es
[6]Assistant Professor, UC3M, Aerospace Engineering Department, jaume.navarro@uc3m.es

the main driver for plasma acceleration and electromagnetic thrust production. The rf power fed to the antenna allows exciting specific electromagnetic modes which mainly depend on the antenna size and geometry. The energy is coupled to the electron population as thermal energy through Helicon wave modes [12] and Trivelpiece-Gould wave modes [13]. The electromagnetic excitation is responsible for ionization and transport phenomena of the charged species, such as ambipolar electric field [14] and diamagnetic electron drift [15], eventually leading to supersonic ion velocities in the MN.

The maturity of this technology is still relatively low [16], therefore prototype characterization and fundamental studies are being conducted on HPTs by many laboratories [3, 9, 11, 17–20]. Thus far, thrust efficiency measurements do not exceed 10 % in many tested devices [3, 8, 21–26], with the only exception of nearly 20 % in the high-power regime [20]. In such a scenario, a deeper insight on the physical phenomena occurring throughout the MN can be obtained via experiments, thus suggesting strategies to performance improvement. The availability of accurate experimental data is a pivotal aspect for the advance in modeling of MN plasma dynamics and thruster design iteration.

Under the typical conditions in terms of power levels and size ranges, ionization cost and wall losses may not represent the only primary source of inefficiency [27]. Given the low input power, the resulting low ionization fraction translates into a dense population of neutrals that inherently impacts the dynamics of the ions to be accelerated. Hence, it is clear that information about the ions and atoms velocity in the MN under different operating conditions, namely power and mass flow rate, is of crucial importance in order to assist the development and validation of more sophisticated kinetic/fluid models [28]. The currently available datasets are limited to a few studies performed on inductive plasma [27] and electron cyclotron resonance (ECR) [29–32] thrusters. Moreover, to the best of the authors knowledge, the velocity profile of neutrals has never been reported in the literature so far.

To this end, the present study reports on the velocity of ions and neutrals in the MN of a HPT. Measurements are performed by means of near-infrared laser-induced fluorescence (LIF) spectroscopy on resonant and metastable states as well as using a Retarding Potential Analyzer (RPA). In the latter case, a rf-compensated Langmuir probe (RFCLP) is required to accurately infer the local plasma potential. The ions and neutrals velocity is spatially resolved from the inside of the discharge chamber up to the far-field plume. Comparative measurements of RPA versus LIF are performed in a single point along the thruster axis for several operating condition so as to explore the widest possible range of ion energy. In the proximity of the thruster exit plane, the intense magnetic field leads to a visible Zeeman and Paschen-Back effects that manifest as a relatively complex shape of the LIF profile. An accurate estimation of the Doppler shift in this region requires a full modeling of the fluorescence profile by accounting for all broadening mechanisms. This strategy is proposed as the unique method to infer the most probable velocity where the magnetic field strength causes the splitting of the probed transitions.

A detailed description of the experimental arrangement is provided in Section II, which includes the HPT, the vacuum facility, the optical setup and the RPA-RFCLP diagnostics kit. Experimental results are presented and discussed in Section III. Fluorescence spectra are introduced first in Section III.A, showing the need of modeling the lineshape. Details of the model are then addressed in Section III.B and eventually theoretical and experimental lineshapes are compared to compute the Doppler shift. The resulting velocity profiles of ions and atoms are reported in Section III.C for a set of operating conditions. The comparison of LIF versus RPA measurements is discussed in Section III.D. Finally, conclusions are drawn in Section IV.

II. Experimental setup

A. Thruster unit and test facility

The thruster unit (TU) studied in this work is schematically depicted in Figure 1. The plasma discharge chamber, also referred to as discharge tube, is made of boron nitride. It is 60 mm long (outlet to injector plate distance), 25 mm in inner diameter and its wall thickness is 1.5 mm. The exit plane of the discharge tube is set as the reference $z = 0$ hereafter. Gas is injected from the back side of the tube through an embedded multi-hole injector, also made in boron nitride, which allows a uniform distribution of the propellant. Both xenon and krypton propellants are investigated in this work.

An assembly of radially polarized Neodymium permanent magnets (PM) generates the desired magnetic field. The PMs are allocated in an auxiliary annular aluminum structure, which allows for a wide flexibility on the assembly configuration, thus enabling the generation of different magnetic field topologies/strengths. In this work, the PMs are assembled to form an annular ring. Since the PMs are radially polarized, they generate a symmetric magnetic field with respect to the mid-plane of the assembly, perpendicular to the z axis in Figure 1. As a consequence, the PMs mid-plane

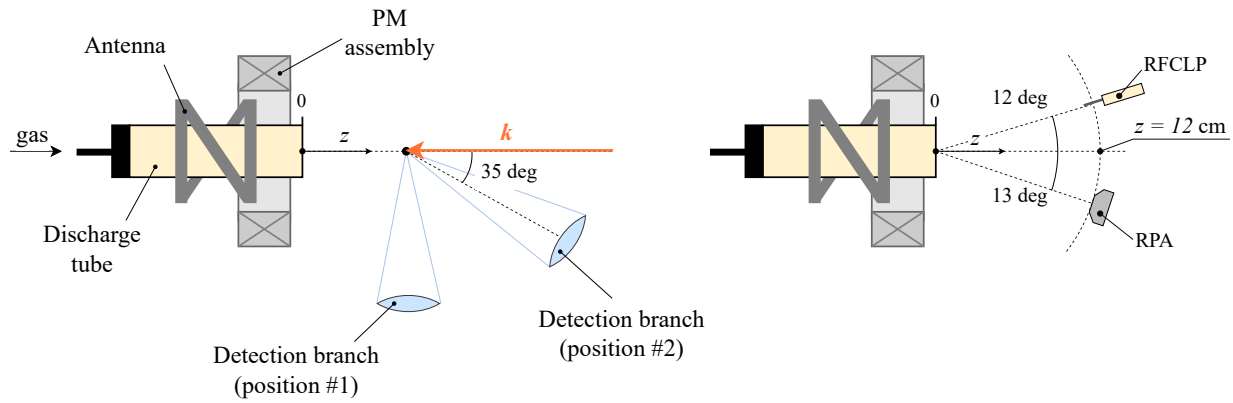

Fig. 1 Experimental setup schematics relative to (left) LIF and (right) RPA measurements. The exit plane of the discharge tube is set as the reference $z = 0$.

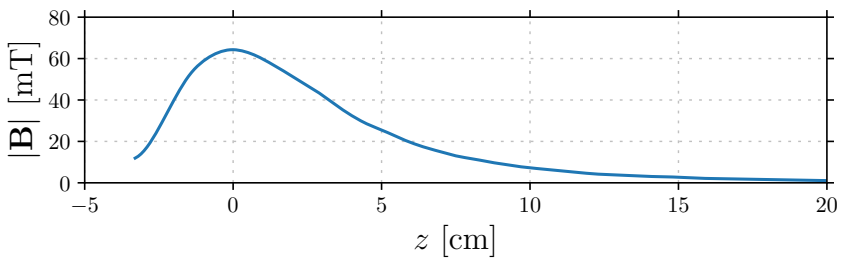

Fig. 2 Axial profile of the HPT magnetic field strength. $z = 0$ refers to the exit plane of the discharge tube.

represents a magnetic separatrix surface. A null field point appears at the center of the assembly. Downstream the separatrix plane, the shape of the magnetic field is convergent-divergent, thus forming the so called MN. Upstream the separatrix plane, the field resembles the same topology because of the mentioned symmetry. The width of the PM annular assembly is 40 mm and the internal radius is 50 mm. Figure 2 shows the magnetic field strength at the centerline of the thruster in the region of interest for the LIF analysis. The peak of the magnetic field reads ≈ 65 mT and coincides with $z = 0$.

Radio-frequency power at 13.56 MHz is fed to the TU through a half-helical silver coated antenna, wrapped around the ceramic tube without entering in physical contact with it. The antenna is 45 mm long and it has a mid diameter of 30 mm. RF power (P_{rf}) is generated with an industrial power amplifier Seren HR2100 and it is conditioned to the antenna with a Sener Aeroespacial S.A. customized L-type matching network and control system [33]. The system can be operated up to 600 W but in this work it has been limited to lower levels.

The thruster unit has been tested inside the main vacuum chamber of the UC3M laboratory. It consists of a non-magnetic stainless-steel vessel of 1.5 m inner diameter and 3.5 m long. The facility background pressure is about 10^{-7} mbar, while the operating pressure is kept within the range $5.9 \times 10^{-6} - 4.6 \times 10^{-5}$ mbar for a Xe flow of 5 to 50 sccm. The vacuum technology implemented in the chamber consists of three cryopanels and a couple of turbomolelucar pumps. The thruster axis is aligned with the vacuum chamber axis, and the thruster outlet section is about 2.5 m away from the chamber downstream wall to minimize plume-chamber wall interactions.

B. Laser-induced fluorescence setup

The atoms and ions velocity is determined by excitation of the probed species via injection of laser beam produced by an amplified tunable single-mode laser diode in the near-infrared spectral range. This measurement technique and the optical apparatus in use have been extensively described in previous works [34, 35]. The laser diode can deliver up to 600 mW in the 810 – 840 nm wavelength range. In the actual experiment, the laser remains mod-hop free over a frequency tuning range larger than 5 GHz. By splitting the primary laser beam into multiple beams, it is possible to: *i*)

Table 1 Xe I, Xe II and Kr II probed optical transitions.

	Transition	λ_{exc} (air)	λ_{fluo} (air)
Xe I	$5p^5(^2P^\circ_{1/2})6s\ ^2[1/2]^\circ_1 \rightarrow$ $\rightarrow 5p^5(^2P^\circ_{1/2})6p\ ^2[3/2]_2$	834.682 17 nm	473.41 nm
Xe II	$5p^4(^3P_2)5d\ ^2[4]_{7/2} \rightarrow$ $\rightarrow 5p^4(^3P_2)6p\ ^2[3]^\circ_{5/2}$	834.724 nm	541.91 nm
Kr II	$4s^24p^4(^3P)4d\ ^4F_{7/2} \rightarrow$ $\rightarrow 4s^24p^4(^3P)5p\ ^2D^\circ_{5/2}$	820.273 nm	461.92 nm

monitor continuously the laser mode and detect any mode hop by means of a Fabry-Pérot interferometer; *ii*) accurately measure the laser wavelength by way of a calibrated wavemeter whose absolute accuracy is 80 MHz ($\approx 60\,\mathrm{m\,s^{-1}}$). Modulation of the laser beam is achieved using a mechanical chopper set at an arbitrary frequency up to a few kHz.

The laser is coupled to a 50 µm multi-mode optical fiber which transports the beam from the optical bench to the inside of the vacuum facility. Here a custom collimator is employed to shine the laser beam in the direction of the thruster axis, cf. Figure 1. At the output of the collimator, the laser beam diameter is about 4 mm, whereas the power density is a few of $\mathrm{mW\,mm^{-2}}$, which ensures a weak saturation effect. Note that $\mathbf{k}\cdot\mathbf{v} < 0$ here, where $\mathbf{k}$ is the laser wavevector and $\mathbf{v}$ the particle velocity. The collimator is kept at a safe distance from the thruster exit plane in order to minimize plume perturbations and avoid overheating. The fluorescence light is collected using a bi-convex lens with 60 mm focal length focusing on a 200 µm core diameter optical fiber. Due to line-of-sight constraints, the detection branch is placed perpendicularly to the laser beam when the measurements are resolved along $z > 0$, whereas it is tilted by 35 deg when scanning at $z < 0$. Both the excitation and detection branches are mechanically linked to a two-axes polar translation stage, whose radial and angular resolutions are 1 mm and 1 deg, respectively. Any relative displacement between the two optical branches is inhibited. The 200 µm optical fiber transports the fluorescence light to a monochromator which isolates the desired line from the whole spectrum. Afterwards, a photomultiplier tube is used to convert the light signal into voltage, which is fed into a lock-in amplifier operating at the laser modulation frequency to distinguish the signal from the natural plasma emission.

The probed optical transitions are reported in Table 1, together with the excitation and fluorescence wavelengths [35–39]. Xenon atoms are probed in the $6s^2[1/2]^\circ$ resonant level, whereas xenon ions are probed in the $5d^2[4]_{7/2}$ metastable level. It is worth mentioning that the LIF signals relative to atoms and ions are collected from distinct frequency tuning scans. In the second part of this work, krypton ions are probed in the $4d^4F_{7/2}$ metastable level.

C. Retarding potential analyzer and RF-compensated Langmuir probe

For the purpose of comparing different diagnostics to infer the ion velocity, a RPA has been designed and manufactured. In the actual configuration, the RPA comprises a series of four stainless-steel grids with holes size of 0.15 mm and a thickness of 0.1 mm. The transparency of each grid is about 25 %. This relatively small mesh size has been achieved through chemical etching and it enables measuring the ion energy in regions where the local plasma density exceeds $10^{17}\mathrm{m^{-3}}$. The grids are labeled using the conventional notation: entrance grid (G1), electron repeller grid (G2), ion filtering grid (G3), and secondary electron repeller grid (G4). A collector (C) made of molybdenum is

(a) **(b)**

Fig. 3 (a) Retarding potential analyzer and (b) RF-compensated Langmuir probe.

placed downstream the grids assembly to enable the ion current measurement. An alumina layer of 0.2 mm thickness is placed between two subsequent grids, functioning both as a spacer and as electrical insulator. The same strategy is employed to insulate G1 and C from the probe housing. By changing the thickness of the multiple alumina layers (while being compliant with the constraints set by the local Debye length), it is possible to add a secondary ion filtering grid with the aim of improving the energy resolution of the probe. The instrument port size is set by an extra metallic layer whose aperture is 5.4 mm in the present configuration. The whole assembly is encapsulated into a non-magnetic stainless-steel body resulting in a probe size of 26 mm in diameter and 11 mm in height. The assembled probe is shown in Figure 3a. The rear side features the electrical connections required to bias the probe elements along with a K-type thermocouple to monitor the probe temperature during operation. The polarization scheme in the present experiment is as follows: G1 at plasma floating potential; G2 at −20 V; G3 swept from −10 V to 65 V with 0.5 V step size; G4 at −70 V; C at −1 V. I-V characteristics are recorded using an automated control unit by Impedans, Ltd. and numerically derivated to retrieve the ion EDF.

Since the ions entering the RPA are accelerated by the plasma sheath that forms at the probe entrance, it is compulsory to measure the local plasma potential V_p to correctly estimate the ion kinetic energy. This task is performed by using a RF-compensated Langmuir probe (RFCLP), which is depicted in Figure 3b. The RF compensation relies on the results and guidelines reported in [40–42]. The probe design makes use of a modular approach so that several different configurations can be tested by replacing each single component. The probe comprises a tip assembly and a main body, which are quickly plugged via a pin connector. The former mainly includes the tip and the auxiliary electrode, whereas the latter contains the chokes series. In the actual configuration, the probe tip is a 0.256 mm tungsten wire with 3 mm length. The tip is inserted into a hypodermic needle and the latter is insulated from a 4 cm^2 auxiliary electrode made of stainless steel through a thin alumina tube. The back end of the compensating electrode is connected to a 4.7 nF axial capacitor. A series of two pairs of chokes is used, each of which is constituted by two inductors self-resonating at one of the first two harmonics. The whole assembly is encapsulated into alumina tubes which accommodate a coaxial connector for probe biasing. I-V curves are recorded using a programmed Source Meter. Thereafter, data are post-processed relying on the orbital motion limited (OML) theory [42, 43]. Assuming local quasineutrality, plasma density is inferred from the linear fit of the ion current squared versus the probe potential. The ion current fit is then subtracted from the total current to obtain a better estimation of the electron current I_e. Eventually, the plasma potential V_p is computed as the probe bias voltage where the first derivative of I_e features its peak value [44].

III. Results and discussion

A. Preliminary considerations on experimental findings

The fluorescence spectra recorded for Xe atoms and ions are shown in Figure 4a and 4b, respectively, for different values of propellant mass flow rate. The density of Xe atoms in the probed resonant state is low due to its short lifetime [37]. As a consequence, the fluorescence signal is rapidly lost downstream the thruster exit plane, therefore the atoms profiles could only be resolved inside the discharge tube and in the near-field region of the plasma plume. Differently, the behavior of Xe ions could be investigated up to 15 cm downstream the exit plane, at the expense of longer integration times to increase the signal-to-noise ratio. The longest time required to scan over one entire profile is in the order of 8 min.

The spectra relative to Xe I, cf. Figure 4a, exhibit a double-peak shape in the region $-2 \lesssim z \lesssim 4.5$ cm. The gap between the two peaks is maximum at $z = 0$, it decreases with z and eventually the peaks merge completely behind the thruster exit plane at $z \simeq 5$ cm. With reference to Figure 4b, a double-peak lineshape is likewise observed also for Xe II in the region close to $z = 0$, i.e. where the magnetic field strength is maximum. In the Xe II profiles, the two peaks merge at $z \simeq 3$ cm and farther downstream the lineshape becomes nearly Gaussian.

Given that these spectra exhibit relatively complex lineshapes nearby the thruster exit plane, the routine assumption that they image the local velocity distribution function (VDF) cannot be applied in this case. The most probable velocity of the probed species is given by the Doppler shift of the line center. However, when the fluorescence light profile does not feature a quasi-Gaussian shape, it is not possible to identify which peak of the profile corresponds to the shifted line center, making it impossible to accurately retrieve the most probable velocity. For this reason, it is necessary to model the expected lineshape by accounting for all the possible broadening mechanisms and fit the experimental profile thus to determine the accurate Doppler shift. Previous experiments relying on LIF spectroscopy have likewise observed a broadening of the recorded spectra, suggesting it was linked either to the Zeeman effect or to charge-exchange (CEX) collisions [31]. The occurrence of a population of slow ions resulting from CEX collisions cannot clarify the profiles

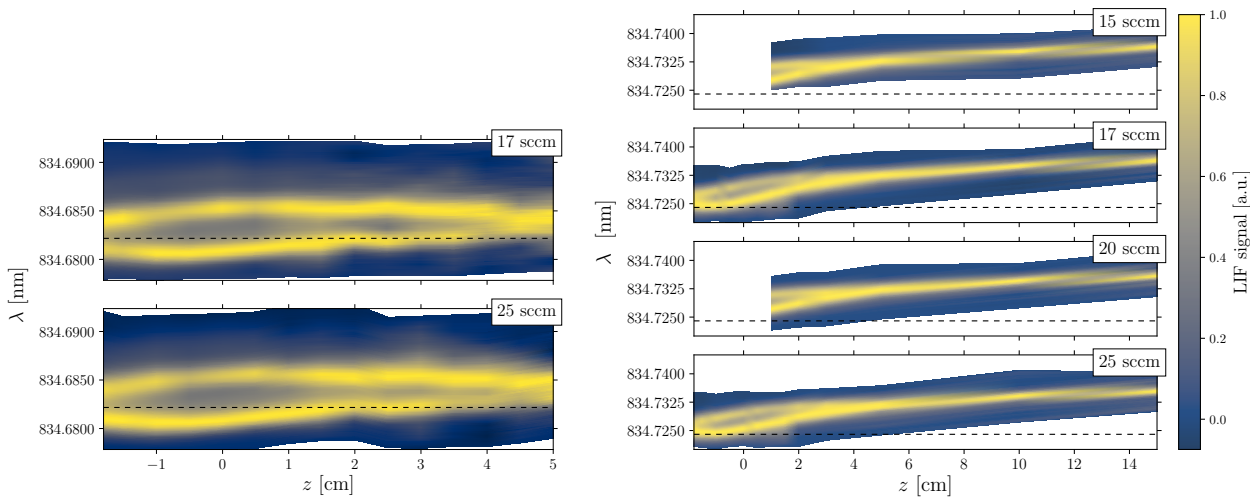

(a) LIF spectra of Xe I resolved along z.

(b) LIF spectra of Xe II resolved along z.

Fig. 4 On-axis LIF spectra of xenon atoms and ions resolved along z. The horizontal dashed line indicates the zero-velocity wavelength, cf. Table 1. Thruster input power is P_{rf} = 350 W.

recorded in this experiment. In fact, this hypothesis would not provide an explanation for the two peaks in the neutrals spectra as well as for the absence of slow ions in the far-field. In Section III.B, modeling of the fluorescence profiles is addressed, proving that the form of measured lineshapes is influenced by the external magnetic field and therefore it results from the Zeeman and Pachen-Back effects.

B. Modeling of fluorescence lineshape

Xenon has seven stable isotopes with abundance above 1 % [45]. Each isotope leads to the so called isotopic shift due to mass and volume differences in the nucleus. Isotopes with odd atomic number (^{129}Xe and ^{131}Xe) possess a non-zero nuclear spin I and therefore lead to the hyperfine structure (HFS). In addition, the presence of a magnetic field further splits each spectral line into several components. As a result, the absorption line comprises several optical transitions. The spectrum is modeled either in the weak or strong field approximation. The former case corresponds to the occurrence of the Zeeman effect, while the latter is referred to as Paschen-Back effect. The choice of relying either on the weak or strong field approximation depends on the local strength of the external magnetic field in the context of the hyperfine interaction [46]. It is quantitatively assessed as customary by comparing the interaction energies associated with the HFS and the magnetic field at each scanning location, i.e.

$$g_J \mu_B |\mathbf{B}|/A \ll 1 \qquad \text{weak field} \tag{1}$$

$$g_J \mu_B |\mathbf{B}|/A \gg 1 \qquad \text{strong field} \tag{2}$$

where g_J is the Landé g-factor, μ_B is the Bohr magneton, A is the magnetic dipole constant and $|\mathbf{B}|$ is the local magnetic field intensity. For what concerns the modeling of Xe I profiles, the weak field approximation is valid as long as the magnetic field intensity remains below ≈ 0.1 T, therefore it represents a justified assumption in the present experiment. Regarding the Xe II lines instead, distinction has to be done in function of the z-coordinate. Indeed, in the proximity of the thruster exit plane, the strong field approximation provides a more realistic picture for the ^{131}Xe lines as long as the magnetic field intensity exceeds ≈ 20 mT.

In practice, the procedure employed to model the fluorescence lineshape needs to be implemented for atoms and ions separately and it consists in:

1) finding all the allowed optical transitions;
2) quantifying the associated detuning frequency;
3) determining the relative intensity of each line;
4) include Doppler broadening and Doppler shift to finally retrieve the lineshape.

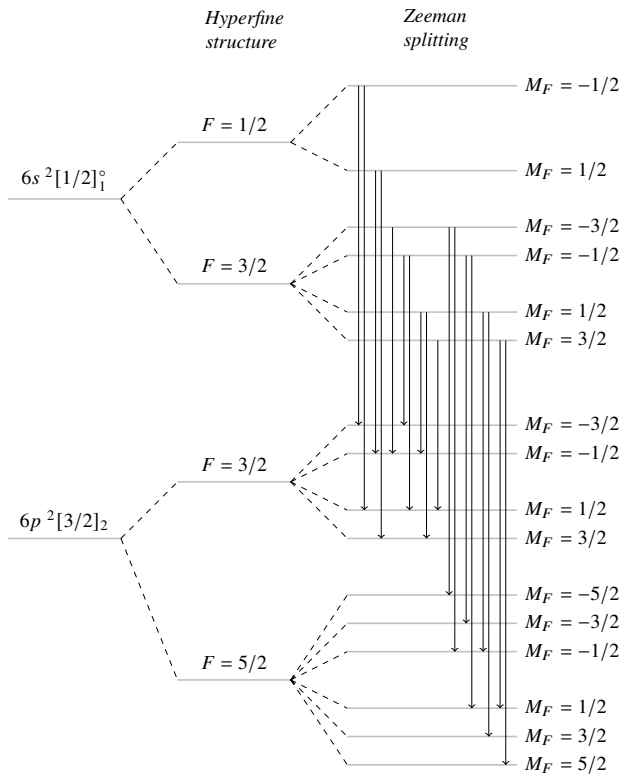

Fig. 5 ^{129}**Xe** σ**-components of the Xe I line at** 834.682 17 nm**.**

In the weak field regime, the upper and lower energy levels of the probed transition are solved by determination of the total angular momentum F and the magnetic M_F quantum numbers for the hyperfine sub-levels, whereas the electronic angular momentum J and the magnetic M_J quantum numbers are required for the even isotopes[36, 37]. The hyperfine components are beforehand identified by the dipole-dipole selection rule $\Delta F = F - F' = [0, \pm 1]$, with $F = 0 \nrightarrow F' = 0$ [46]. In the strong field case, F and M_F are undefined quantum numbers therefore the set (I, J, M_I, M_J) needs to be used instead. The allowed transitions are set by the values of $\Delta M_{F,J}$. The latter are selected by accounting for the laser polarization with respect to the magnetic field vector. As the polarization at at the output of the optical fiber is negligible, when the laser is shone in the direction of the magnetic field ($\mathbf{k} \parallel \mathbf{B}$), only the σ components ($\Delta M_{F,J} = \pm 1$) are allowed. Though, when $\mathbf{k} \nparallel \mathbf{B}$, both σ and π components ($\Delta M_{F,J} = 0$) need to be accounted for. The selection rule $\Delta M_I = 0$ is additionally considered whenever the strong field condition is met. In the simplest case when only the σ components are allowed and the weak field approximation holds, the selection rules lead to 6 lines for each even isotope, 18 for ^{129}Xe and 54 for ^{131}Xe in the $6s\ ^2[1/2]^\circ_1 \rightarrow 6p\ ^2[3/2]_2$ transition of Xe I. Regarding the $5d\ ^2[4]_{7/2} \rightarrow 6p\ ^2[3]^\circ_{5/2}$ transition of Xe II instead, the spectrum comprises 12 lines for the each even isotope, 36 for ^{129}Xe and 108 for ^{131}Xe. An instance of the allowed σ transitions due to hyperfine structure and Zeeman effect is shown in Figure 5 for ^{129}Xe isotope relative to the Xe I line at 834.682 17 nm. Several additional lines appear when the π components are included.

The energy shift of each transition is computed as the sum of three terms: the isotopic shift ΔE_{IS}, the contribution of the hyperfine structure ΔE_{hfs}, the contribution of the Zeeman effect ΔE_Z. The values of ΔE_{IS} for the Xe I and Xe II lines here investigated are tabulated in [47] and [48], respectively. It is chosen to refer these shifts to ^{132}Xe since it is the most abundant isotope. The hyperfine structure term ΔE_{hfs} is nonzero for the odd isotopes only and it is the sum of magnetic dipole and electric quadrupole contributions [36, 46, 49]. The latter are function of the hyperfine constants A and B which can be found in [36, 50] for the two transitions used in this work. The last contribution to the total energy shift, i.e. ΔE_Z, is a function of the magnetic quantum number $M_{F,J,I}$, the strength of the magnetic field and the Landé g-factor g_F or g_J, depending on the isotope atomic number and weak/strong field regime. Complete expressions for ΔE_{hfs}, ΔE_Z and g_F can be found in [46]. The values of g_J and the nuclear magnetic dipole moments μ_I necessary to compute g_F are provided in [39, 51].

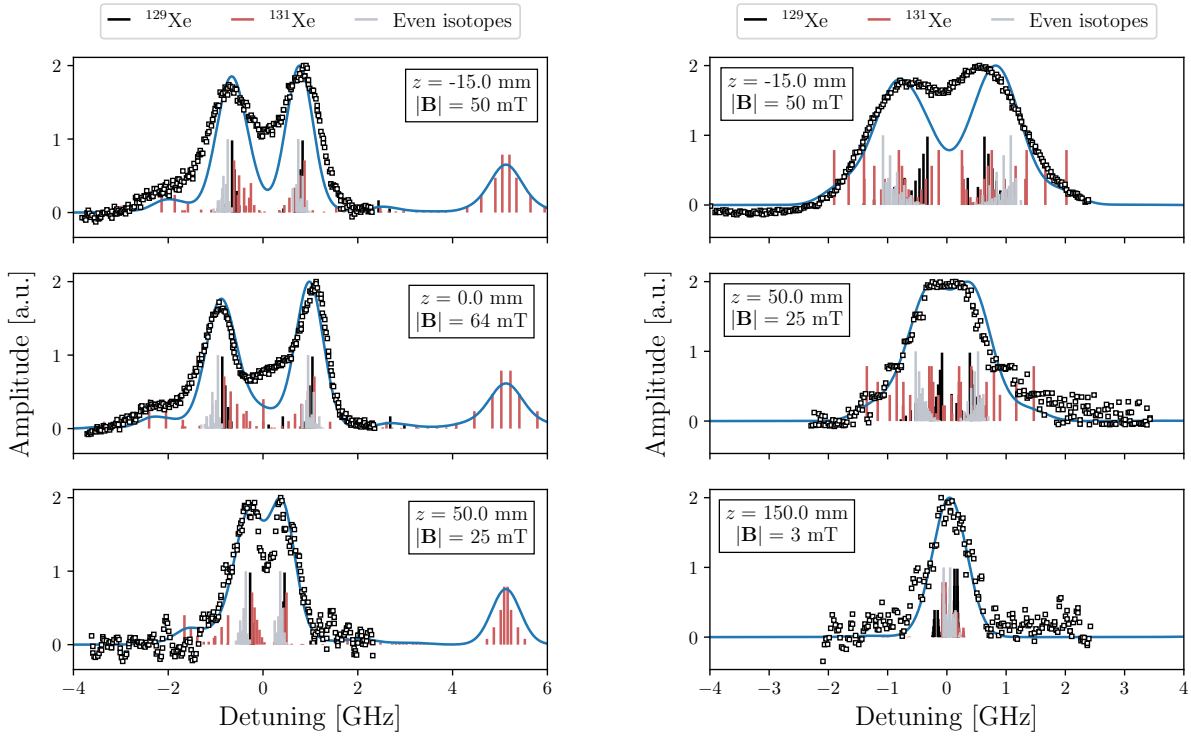

(a) Experimental (scatter points) and modeled (solid line) lineshape for the $6s\,^2[1/2]^\circ_1 \rightarrow 6p\,^2[3/2]_2$ transition of Xe I.

(b) Experimental (scatter points) and modeled (solid line) lineshape for the $5d\,^2[4]_{7/2} \rightarrow 6p\,^2[3]^\circ_{5/2}$ transition of Xe II.

Fig. 6 Experimental (squares) and modeled (line) lineshape for (a) Xe I and (b) Xe II transitions. The experimental data points are Doppler shifted to fit the model profile. Thruster operation parameters are: 350 W**, 25 sccm.**

After the energy shift of each transition is known, the complete spectrum is built by determining the relative intensity. The equations of interest are reported in [46] for each of the π and σ components[a]. They are function of F and M_F (J and M_J) for the odd (even) isotopes. The so computed intensities require to be weighted accounting for natural abundance of each isotope [45] and hyperfine components tabulated in [52] as a function of I, ΔJ and ΔF. Furthermore, in order to account for the laser polarization direction, the intensity of each π transition can be scaled by $\sin(\theta)$, where θ is the local relative angle between **k** and **B**.

At last, Doppler broadening of each transition is addressed. At this stage, two reasonable approximations are made: the laser beam profile is considered as a Dirac delta function due to its bandwidth (< 1 MHz), and the natural width (5 MHz) is neglected in comparison to the Doppler broadening full width at half maximum ($\simeq$ 0.65 GHz at T = 800 K) [37]. It is assumed that ions and atoms share the same temperature. A Gaussian profile is applied to each component, exhibiting identical width and frequency shift. Eventually, the theoretical lineshape stems from the sum of all individual Gaussian profiles.

Figures 6a and 6b illustrate two sets of the model outcomes compared to the experimental LIF spectra recorded in different locations of the plasma beam for atoms and ions, respectively. These spectra comprise the σ transitions only as **k** $\parallel$ **B**. A kinetic temperature of 800 K is used to fit the experimental profiles, which are Doppler shifted to overlap the model lineshape. It is observed that a portion of the Xe I spectrum has not been included in the experimental scan, cf. Figure 6a. However, this fact is irrelevant considering that the focus here is on the Doppler shift. A poorly satisfactory match in the 0 GHz region is found for those profiles that exhibit a double-peak shape, for both Xe I and Xe II. In relation to this matter, the size of the laser beam and its alignment are possibly involved. The model

[a]The results are obtained by direct substitution of $|J\,M_J\rangle$ and $|F\,M_F\rangle$ in the equations reported in [46]. The extent to which these intensities are approximations was not explored here.

reasonably assumes that the excitation light is perpendicularly polarized with respect to the magnetic field. Yet, a slight misalignment and/or a relatively large probed volume would enable the occurrence of π transitions. The intensity of these transitions would be related to the angle between **k** and **B**. Nevertheless, it is virtually impossible to quantify this contribution. By manually implementing a non-zero angle between **k** and **B** in the simulation code, it is found that a misalignment in the order of $2-3$ deg is sufficient to visibly alter the 0 GHz region. These values are perfectly compatible with the uncertainty associated with the experimental setup and the magnetic field simulation accuracy.

The most probable velocity is ultimately estimated from direct implementation of the Doppler shift equation [35]. This shift is equal to the off-set in the frequency axis that gives the best match between the experimental and modeled lineshapes with a precision of 10 MHz ($\approx 8\ \mathrm{m\,s^{-1}}$). This procedure is clearly embedded in the simulation algorithm. The reference zero-velocity frequency ν_0 comes from previous experiments reported in [36] relying on two-beam saturated spectroscopy in a drift-free RF plasma. Altogether, this technique allows deducing the kinetic temperature and the most probable velocity with a reasonable accuracy. The error bar results from several contributing factor, such as the uncertainty on hyperfine constants and isotopic shifts in input, the quality of the raw data, the robustness of the fitting algorithm. Although the signal-to-noise ratio decreases downstream, the single-peak shape of the recorded profiles simplifies the fitting procedure. By exploring the full range of uncertainties of the input constants to the model (i.e. isotopic shifts and hyperfine constants) and different filtering parameters on the noisy signals, it is estimated that the typical uncertainty is in the order of $\pm 10\ \mathrm{m\,s^{-1}}$ and ± 100 K for the velocity and temperature, respectively.

C. Atoms and ions velocity profiles

The velocity profiles of Xe and Xe^+ herein reported are extracted by means of the model illustrated in Section III.B. The value of the kinetic temperature is fixed to 800 K for both species since it fits well the experimental data.

Figure 7 displays the evolution of the atoms axial velocity along the thruster center line. This data is deduced from the LIF spectra in Figure 4a. It is found that the neutrals drift towards the exit plane with a velocity smaller than the thermal speed ($v_{th} = \sqrt{8k_BT_i/\pi m_i} \approx 365\ \mathrm{m\,s^{-1}}$ at 800 K). Then, the atom velocity increases within a few centimeters over the thruster exit plane up to $700-800\ \mathrm{m\,s^{-1}}$. Note that at 800 K and with $\gamma = 5/3$, the sound speed reads $v_s = \sqrt{\gamma k_BT_i/m_i} \approx 295\ \mathrm{m\,s^{-1}}$. Thus, the neutrals reach the sonic point in the proximity of the thruster outlet and expand supersonically within the plume. This behavior is not visibly influenced by a different value of the propellant mass flow rate. Similar upper values of the neutrals axial velocity have been found also in Hall thrusters [37]. This relatively high speed of the atoms is likely to result from various contributing phenomena. Inside the discharge chamber, the ions naturally recombine at the walls. They are reflected back with a fraction of the momentum carried before the recombination and therefore populate the high energy wing of the atoms distribution function. Ion-neutral elastic collisions may likewise contribute to increase the most probable atom velocity. The neutrals largely dominate the discharge chamber with a particle density of $\sim 10^{20}\ \mathrm{m^{-3}}$, derived from mass flow conservation and assumed uniform everywhere. As a result, the mean free path for ion-neutral momentum transfer collisions reads $\lambda \simeq 3.5$ mm using an equivalent cross section $\sigma_{el} = 2\times 10^{-18}\ \mathrm{m^2}$ at about 1 eV of ion energy [53]. For comparison, the cross section associated with CEX collisions reads $\sigma_{CEX} \simeq 0.8\times 10^{-18}\ \mathrm{m^2}$ [54], thus showing that elastic collisions are about 2.5 times more likely that CEX collisions. Furthermore, the slow wing of the atoms distribution function is selectively depopulated in the high electron density region, i.e. close to the magnetic nozzle throat, due to the relatively longer residence time that leads to higher ionization probability.

The profiles of the ions axial velocity are reported in Figure 8a and 8b for several values of the propellant mass flow rate and input power, respectively. For all the tested working points, it can be noticed that the ions still experience a non-negligible momentum gain several centimeters downstream the thruster exit plane. The evolution of the ion velocity at $z \lesssim 2$ cm is not visibly influenced by the thruster working condition. Indeed, all the profiles tend to merge close to the thruster exit plane. The ions leave the discharge chamber with a drift velocity of about $1.4\ \mathrm{km\,s^{-1}}$. Assuming a conservative value of the local electron temperature of $4-5$ eV at $z = 0$ according to previous measurements taken in a similar device [3, 26], the Bohm speed equals $1.7-1.9\ \mathrm{km\,s^{-1}}$. It clearly means that the sonic condition is reached downstream the throat of the magnetic field, in contrast with the ideal gas-dynamics analogy of the plasma expansion as routinely postulated in fluid models[14, 55]. Previous experiments performed on other devices [11, 27, 30–32] have similarly observed a subsonic ion flow in correspondence of the magnetic nozzle throat. In this experiment, by accounting for positioning uncertainties in the experimental setup, the axial shift of the sonic transition is in the order of several millimeters, which is consistent with the findings reported in [30, 31]. Given that a single population of ions dominates the LIF spectra in this experiment, CEX collisions cannot explain the shifting of the sonic point. On the other hand, ion-neutral elastic collisions, electron-neutral collisions and ionization within the plume may represent

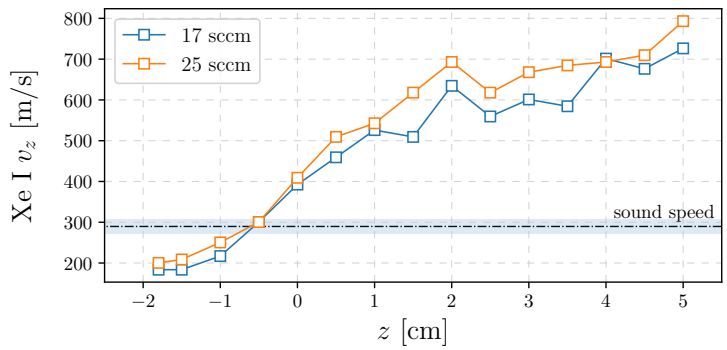

Fig. 7 Axial velocity profile of Xe I for different propellant mass flow rates. Dash-dotted line indicates the sonic speed at T = 800 K, shaded area delimitates the ±100 K uncertainty interval. Thruster operating parameters are: 350 W, (blue) 17 sccm, (orange) 25 sccm.

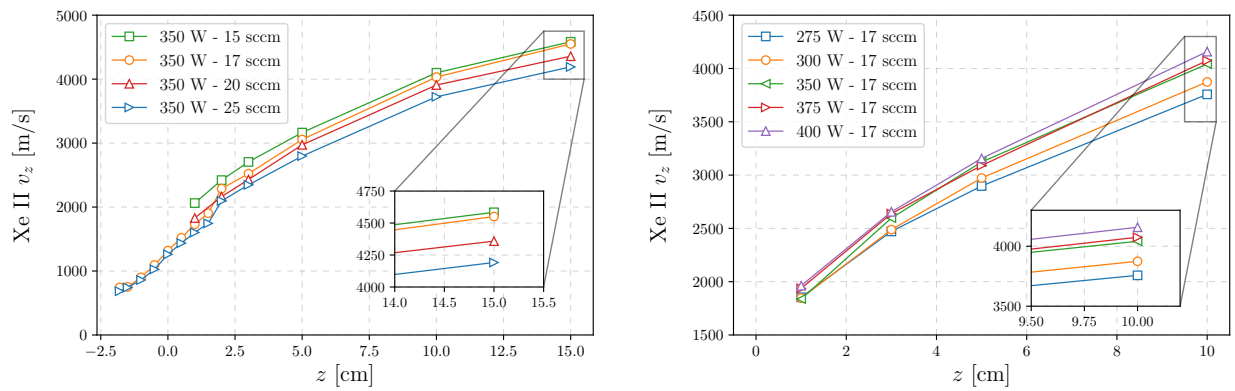

(a) Xe II axial velocity for different propellant mass flow rates. **(b) Xe II axial velocity for different levels of input power.**

Fig. 8 Axial velocity profile of Xe II for different operating parameters.

a pivotal explanation to the axial shift of the sonic transition [27, 32]. The occurrence of ion-neutral collisions is compatible with the observed atom velocity profiles shown in Figure 7, as previously discussed.

The effect of a different working point of the thruster becomes more evident far downstream, cf. Figure 8a and Figure 8b. A larger ultimate velocity is recorded at lower mass flow rates and higher input powers. Altogether, the highest value of the ion axial velocity reads about 4600 m s^{-1} at z = 15 cm, obtained for 350 W and 15 sccm.

D. Comparison of RPA and LIF spectroscopy results

The ion beam energy is additionally probed using the RPA described in Section II.C for the purpose of comparing the two measurement techniques. A consequence of the discussion reported in Section III.A and III.B is that the intense magnetic field in the close-field region prevents a direct comparison of the ion VDF retrieved with the two diagnostics simply because the LIF profile does not picture the true ion VDF. For this reason, measurements are performed and compared at a single point far downstream where the RPA does not substantially interfere with the plasma beam and the fluorescence signal still manifests a good signal-to-noise ratio while being negligibly altered by the magnetic field. The choice of a single point also stems from the fact that an extended scan, either along the axial or angular direction, is prohibited by alignment limitations due the nature of the radial-polar translation system whenever multiple probes are employed (RPA and RFCLP in this particular case).

In short, the experimental setup related to the RPA measurements is schematically depicted in Figure 1. The RPA and the RFCLP are mounted on the translation stage in such a way that they are both aligned with the thruster axis at z = 12 cm. Data from the two probes are acquired nearly simultaneously after prior rotation of the arm system to ensure

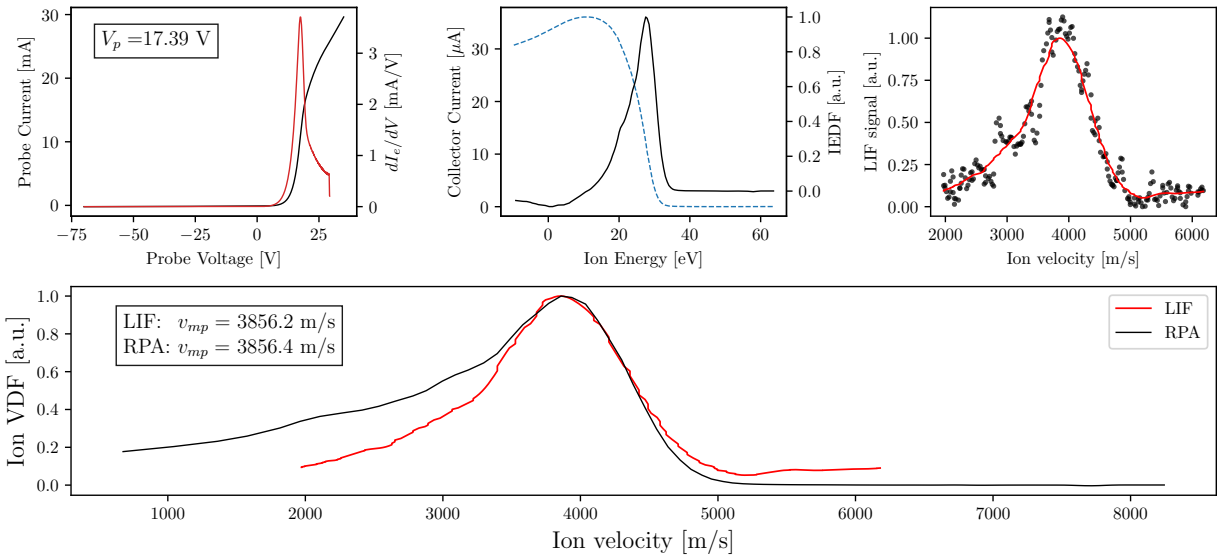

Fig. 9 Example of dataset acquired to compare LIF and RPA measurements. (top-left) Langmuir probe I-V curve and I_e derivative, (top-center) RPA I-V curve and its derivative, (top-right) LIF spectrum, (bottom) ion VDF comparison. Thruster operation parameters are: P_{rf} = 350 W, $\dot{m}$ = 20 sccm Xe.

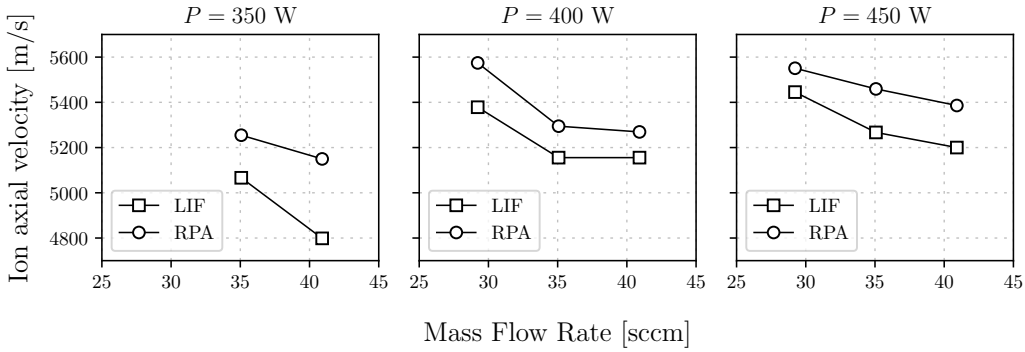

Fig. 10 Most probable axial velocity of Kr ions probed with RPA and LIF at different levels of P_{rf} and $\dot{m}$.

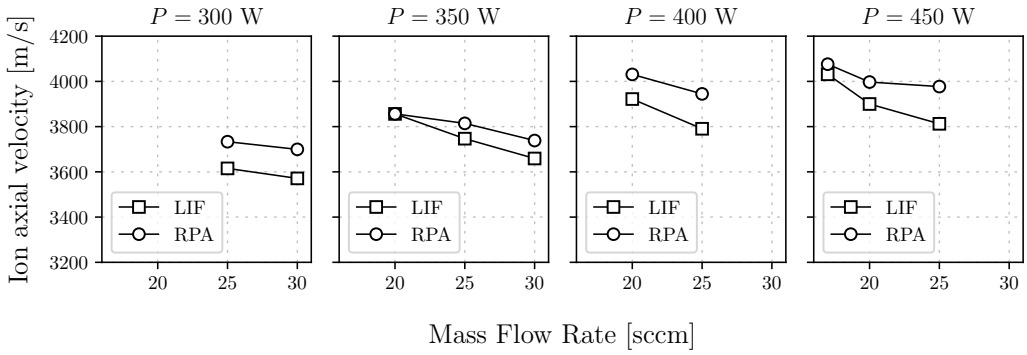

Fig. 11 Most probable axial velocity of Xe ions probed with RPA and LIF at different levels of P_{rf} and $\dot{m}$.

proper alignment of each probe. It shall be remarked that LIF and RPA measurements are performed over different days. The TU is operated with both krypton and xenon propellants under different values of input power and mass flow rate. For each operational point, the associated dataset comprises of an I-V curve from the RFCLP, an I-V curve from the RPA and a fluorescence profile from LIF, as exemplified in Figure 9. The resulting axial ion velocity probed with the two instruments is plotted in Figure 10 and 11 for krypton and xenon, respectively. These values are extracted from the LIF and RPA velocity profiles in correspondence of the peak, therefore they represent the most probable axial velocity. It is observed that the two measurement techniques are in reasonably good agreement. In general, the ion velocity determined with the RPA always results larger than that measured with LIF spectroscopy. The mean difference between the two measurements is $184.0\,\mathrm{m\,s^{-1}}$ with a standard deviation of $71.9\,\mathrm{m\,s^{-1}}$ when operating the thruster with krypton, whereas a mean difference of $96.3\,\mathrm{m\,s^{-1}}$ with a standard deviation of $47.7\,\mathrm{m\,s^{-1}}$ are observed in the case of xenon. These discrepancies are close to the accuracy of the LIF setup set by the wavemeter resolution. From Figure 9, it can be deduced that the ion VDF from both LIF and RPA is slightly asymmetric, which is possibly due to the presence of slow ions. These can result from ion-neutral and charge-exchange collisions, as previously discussed in Section III.C. However, a detailed comparison of the VDF resulting from the two techniques is out of the scope of this study because several phenomena contribute altering its shape. Indeed, hyperfine structure and magnetic field do not allow measuring the unperturbed ion VDF using LIF, whereas the I-V curve from the RPA is sensitive to the specific device, the presence of secondary electrons, ionization and charge-exchange collisions occurring inside the probe.

IV. Conclusion

Plasma flow velocity has been spatially resolved using laser-induced fluorescence spectroscopy and a retarding potential analyzer in the magnetic nozzle of a Helicon plasma thruster operating under several conditions. The most probable ion axial velocity obtained with two instruments is compared in a single point of the far-field plume when the thruster operates with Xe and Kr propellants. It is found that the two diagnostics are in good agreement. In all tested conditions, the ion velocity measured with the RPA is larger than that resulting from LIF. The mean relative difference between the two techniques is in the order of $2-3\,\%$ accounting for all explored operating conditions.

Xenon atoms and ion dynamics is studied inside and outside the discharge chamber via LIF. In the near-field plume, the intense magnetic field induces the Zeeman effect, leading to a relatively complex shape of the fluorescence spectra. Consequently, it results impossible to accurately deduce the atoms and ions velocity in the strong magnetic field region without prior modeling of the atomic lineshape. Hence, this task is addressed by accounting for broadening mechanisms, namely isotopic shift, hyperfine structure and Zeeman effect. Fitting of the modeled and measured profiles allowed inferring the evolution of the most probable velocity both for the Xe atoms and ions. It is found that the neutrals axial velocity increases up to supersonic values downstream the thruster exit plane. This phenomenon is associated with parallel occurrence of several processes. The fast atoms wing of the distribution function is populated because of flow expansion, ions recombination at the walls and ion-neutral momentum transfer collisions, whereas the slow atoms wing is selectively depopulated because of ionization. The axial evolution of the ions velocity uncovers the effect of the thruster working parameters. Faster ions are obtained at lower mass flow rates and higher levels of input power. The velocity profiles also show that the acceleration region extends several centimeters downstream the exit plane. The largest Xe ion velocity recorded in the probed region is about $4600\,\mathrm{m\,s^{-1}}$ at $z = 15$ cm for 350 W of input power and 15 sccm of mass flow rate.

The experimental findings reported in this paper contribute to advance in understanding the ions and atoms dynamics in a magnetic nozzle. Development and validation of numerical models can largely benefit from the data herein presented. A parallel numerical and experimental investigation of the near-field atom and ion dynamics under different working conditions would further assist in clarifying the current picture. Implementation of collisions and wall recombination phenomena in particle-in-cell models is particularly advised. It is clearly of interest to conduct a system parametric analysis targeting a larger ultimate ion velocity in view of developing an efficient electric propulsion system.

Acknowledgments

This project has received funding from the European Unions Horizon 2020 research and innovation program under grant agreement No 870542 (HelIcon PlasmA Thruster for In-space Applications) and Diagnosis ToolKit project (SENER-UC3M-CNRS) under ESA-TDE program. This work was also carried out in the frame of the Santander Chair of Excellence from the Carlos III University in Madrid granted to Dr. S. Mazouffre in 2020.

References

[1] O'reilly, D., Herdrich, G., and Kavanagh, D. F., "Electric propulsion methods for small satellites: A review," *Aerospace*, Vol. 8, No. 1, 2021, pp. 1–30. https://doi.org/10.3390/aerospace8010022.

[2] Bathgate, S. N., Bilek, M. M., and McKenzie, D. R., "Electrodeless plasma thrusters for spacecraft: A review," *Plasma Science and Technology*, Vol. 19, No. 8, 2017. https://doi.org/10.1088/2058-6272/aa71fe.

[3] Navarro-Cavallé, J., Wijnen, M., Fajardo, P., and Ahedo, E., "Experimental characterization of a 1 kW Helicon Plasma Thruster," *Vacuum*, Vol. 149, 2018, pp. 69–73. https://doi.org/10.1016/j.vacuum.2017.11.036.

[4] Takahashi, K., "Helicon-type radiofrequency plasma thrusters and magnetic plasma nozzles," *Reviews of Modern Plasma Physics*, Vol. 3, Springer Singapore, 2019. https://doi.org/10.1007/s41614-019-0024-2, URL https://doi.org/10.1007/s41614-019-0024-2.

[5] Packan, D., Elias, P., Jarrige, J., Vialis, T., Correyero, S., Peterschmitt, S., Porto-Hernandez, J.-C., Merino, M., Sánchez-Villar, A., Ahedo, E., Peyresoubes, G., Thorinius, A., Denis, S., Holste, K., Klar, P., Scharmann, S., Zorn, J., Bekemans, M., Scalais, T., Bourguignon, E., Zurbach, S., Azais, P., Habbassi, I., Mares, M., and Hoque, A., "H2020 MINOTOR : Magnetic Nozzle Electron Cyclotron Resonance Thruster," *36th International Electric Propulsion Conference*, 2019.

[6] Wachs, B., and Jorns, B., "Technique for Two-Frequency Optimization of an ECR Magnetic Nozzle Thruster," *International Electric Propulsion Conference*, 2019, pp. 1–11.

[7] Peterschmitt, S., and Packan, D., "Comparison of Waveguide Coupled and Coaxial Coupled ECRA Magnetic Nozzle Thruster using a Thrust Balance," *International Electric Propulsion Conference*, 2019. URL https://hal.archives-ouvertes.fr/hal-02344365.

[8] Bellomo, N., Magarotto, M., Manente, M., Trezzolani, F., Mantellato, R., Cappellini, L., Paulon, D., Selmo, A., Scalzi, D., Minute, M., Duzzi, M., Barbato, A., Schiavon, A., Di Fede, S., Souhair, N., De Carlo, P., Barato, F., Milza, F., Toson, E., and Pavarin, D., "Design and In-orbit Demonstration of REGULUS, an Iodine electric propulsion system," *CEAS Space Journal*, , No. 0123456789, 2021. https://doi.org/10.1007/s12567-021-00374-4, URL https://doi.org/10.1007/s12567-021-00374-4.

[9] Romano, F., Herdrich, G., Traub, C., Fasoulas, S., Crisp, N., Edmondson, S., Haigh, S., Livadiotti, S., Oiko, V. T. A., Sinpetru, L. A., Smith, K., Becedas, J., Bisgaard, M., Christensen, S., Hanessian, V., Jensen, T. K., Nielsen, J., Sureda, M., Kataria, D., Belkouchi, B., Conte, A., Seminari, S., Road, O., Deimos, E., Systems, S., and Space, M., "Design , Set-Up , and First Ignition of the RF Helicon-based Plasma Thruster," *Space Propulsion Conference 2020+1*, 2021.

[10] Furukawa, T., Kuwahara, D., and Shinohara, S., "Spatial characteristics of rotating magnetic field (RMF) plasma acceleration method in open magnetic field configuration under partial RMF penetration," *Physics of Plasmas*, Vol. 28, No. 073507, 2021. https://doi.org/10.1063/5.0035383.

[11] Vinci, A. E., and Mazouffre, S., "Plasma properties conditioned by the magnetic throat location in a helicon plasma device," *Journal of Applied Physics*, Vol. 130, No. 183301, 2021. https://doi.org/10.1063/5.0069983.

[12] Light, M., Sudit, I. D., Chen, F. F., and Arnush, D., "Axial propagation of helicon waves," *Physics of Plasmas*, Vol. 2, No. 11, 1995, pp. 4094–4103. https://doi.org/10.1063/1.871032.

[13] Blackwell, D. D., Madziwa, T. G., Arnush, D., and Chen, F. F., "Evidence for Trivelpiece-Gould Modes in a Helicon Discharge," *Physical Review Letters*, Vol. 88, No. 14, 2002, p. 4. https://doi.org/10.1103/PhysRevLett.88.145002.

[14] Ahedo, E., and Merino, M., "Two-dimensional supersonic plasma acceleration in a magnetic nozzle," *Physics of Plasmas*, Vol. 17, No. 7, 2010, pp. 1–15. https://doi.org/10.1063/1.3442736.

[15] Takahashi, K., Chiba, A., Komuro, A., and Ando, A., "Experimental identification of an azimuthal current in a magnetic nozzle of a radiofrequency plasma thruster," *Plasma Sources Science and Technology*, Vol. 25, No. 5, 2016, p. 55011. https://doi.org/10.1088/0963-0252/25/5/055011, URL http://dx.doi.org/10.1088/0963-0252/25/5/055011.

[16] Dale, E., Jorns, B., and Gallimore, A., "Future Directions for Electric Propulsion Research," *Aerospace*, Vol. 7, No. 120, 2020.

[17] Shinohara, S., Kuwahara, D., Ishigami, Y., Horita, H., and Nakanishi, S., "Extremely small-diameter, high-density, radio frequency, plasma sources and central gas feeding for next-generation electrodeless plasma thrusters," *Review of Scientific Instruments*, Vol. 91, No. 073507, 2020.

[18] Vinci, A. E., and Mazouffre, S., "Direct experimental comparison of krypton and xenon discharge properties in the magnetic nozzle of a helicon plasma source," *Physics of Plasmas*, Vol. 28, No. 033504, 2021. https://doi.org/10.1063/5.0037117.

[19] Vinci, A. E., DelavièreDelion, Q., and Mazouffre, S., "Electron thermodynamics along magnetic nozzle lines in a helicon plasma," *Journal of Electric Propulsion*, Vol. 1, No. 4, 2022. https://doi.org/10.1007/s44205-022-00003-0.

[20] Takahashi, K., "Magnetic nozzle radiofrequency plasma thruster approaching twenty percent thruster efficiency," *Scientific Reports*, Vol. 11, No. 1, 2021, pp. 1–12. https://doi.org/10.1038/s41598-021-82471-2, URL https://doi.org/10.1038/s41598-021-82471-2.

[21] Takahashi, K., Lafleur, T., Charles, C., Alexander, P., Boswell, R. W., Perren, M., Laine, R., Pottinger, S., Lappas, V., Harle, T., and Lamprou, D., "Direct thrust measurement of a permanent magnet helicon double layer thruster," *Applied Physics Letters*, Vol. 98, No. 14, 2011, pp. 2–4. https://doi.org/10.1063/1.3577608.

[22] Williams, L. T., and Walker, M. L., "Thrust measurements of a helicon plasma source," *47th AIAA/ASME/SAE/ASEE Joint Propulsion Conference and Exhibit 2011*, 2011, pp. 1–15. https://doi.org/10.2514/6.2011-5893.

[23] Pottinger, S., Lappas, V., Charles, C., and Boswell, R., "Performance characterization of a helicon double layer thruster using direct thrust measurements," *Journal of Physics D: Applied Physics*, Vol. 44, No. 23, 2011. https://doi.org/10.1088/0022-3727/44/23/235201.

[24] Takahashi, K., Charles, C., Boswell, R., and Ando, A., "Performance improvement of a permanent magnet helicon plasma thruster," *Journal of Physics D: Applied Physics*, Vol. 46, No. 35, 2013. https://doi.org/10.1088/0022-3727/46/35/352001.

[25] Takahashi, K., Takao, Y., and Ando, A., "Thrust imparted by a stepped-diameter magnetic nozzle rf plasma thruster," *Applied Physics Letters*, Vol. 113, No. 3, 2018. https://doi.org/10.1063/1.5041034.

[26] Navarro-Cavallé, J., Wijnen, M., Fajardo, P., Ahedo, E., Gomez, V., Giménez, A., and Ruiz, M., "Development and Characterization of the Helicon Plasma Thruster Prototype HPT05M," *36th International Electric Propulsion Conference*, 2019.

[27] Collard, T. A., and Jorns, B. A., "Magnetic nozzle efficiency in a low power inductive plasma source," *Plasma Sources Science and Technology*, Vol. 28, No. 10, 2019. https://doi.org/10.1088/1361-6595/ab2d7d.

[28] Martinez-Sanchez, M., Navarro-Cavallé, J., and Ahedo, E., "Electron cooling and finite potential drop in a magnetized plasma expansion," *Physics of Plasmas*, Vol. 22, No. 5, 2015, pp. 1–12. https://doi.org/10.1063/1.4919627.

[29] Jarrige, J., Correyero, S., Elias, P.-Q., and Packan, D., "Investigation on the ion velocity distribution in the magnetic nozzle of an ECR plasma thruster using LIF measurements," *International Electric Propulsion Conference*, 2017, pp. 1–10.

[30] Correyero, S., Jarrige, J., Packan, D., and Ahedo, E., "Ion acceleration in the magnetic nozzle of an ECR thruster: Comparison of experimental measurements with a quasi 1D kinetic model," *Space Propulsion 2018*, , No. May, 2018, pp. 1–8.

[31] Correyero, S., Jarrige, J., Packan, D., Ahedo, E., Correyero, S., Jarrige, J., Packan, D., and Ahedo, E., "Plasma beam characterization along the magnetic nozzle of an ECR thruster," *Plasma Sources Sci. Technol.*, Vol. 28, No. 9, 2019.

[32] Wachs, B., and Jorns, B., "Background pressure effects on ion dynamics in a low-power magnetic nozzle thruster," *Plasma Sources Science and Technology*, Vol. 29, No. 4, 2020. https://doi.org/10.1088/1361-6595/ab74b6.

[33] Gomez, V., Giménez, A., Ruiz, M., Navarro-Cavallé, J., Fajardo, P., Wijnen, M., and Ahedo, E., "RF Power - Plasma Coupling Experimental Results in a Helicon Plasma Thruster Prototype," *36th International Electric Propulsion Conference*, 2019.

[34] Mazouffre, S., Kulaev, V., and Luna, J. P., "Ion diagnostics of a discharge in crossed electric and magnetic fields for electric propulsion," *Plasma Sources Science and Technology*, Vol. 18, No. 3, 2009. https://doi.org/10.1088/0963-0252/18/3/034022.

[35] Mazouffre, S., "Laser-induced fluorescence diagnostics of the cross-field discharge of Hall thrusters," *Plasma Sources Science and Technology*, Vol. 22, No. 1, 2012. https://doi.org/10.1088/0963-0252/22/1/013001.

[36] Pawelec, E., Mazouffre, S., and Sadeghi, N., "Hyperfine structure of some near-infrared Xe I and Xe II lines," *Spectrochimica Acta - Part B Atomic Spectroscopy*, Vol. 66, No. 6, 2011, pp. 470–475. https://doi.org/10.1016/j.sab.2011.05.009.

[37] Mazouffre, S., Bourgeois, G., Garrigues, L., and Pawelec, E., "A comprehensive study on the atom flow in the cross-field discharge of a Hall thruster," *Journal of Physics D: Applied Physics*, Vol. 44, No. 10, 2011. https://doi.org/10.1088/0022-3727/44/10/105203.

[38] Lejeune, A., Bourgeois, G., and Mazouffre, S., "Kr II and Xe II axial velocity distribution functions in a cross-field ion source," *Physics of Plasmas*, Vol. 19, No. 7, 2012. https://doi.org/10.1063/1.4731688.

[39] Kramida, A., Ralchenko, Y., Reader, J., and Team, N. A., "NIST Atomic Spectra Database (ver. 5.8), [Online]. Available: https://physics.nist.gov/asd [2021, September 16]. National Institute of Standards and Technology, Gaithersburg, MD." , 2020.

[40] Sudit, I. D., and Chen, F. F., "RF Compensated Probes for High-density Discharges," *Plasma Sources Science and Technology*, Vol. 3, No. 2, 1994, pp. 162–168. https://doi.org/10.1088/0963-0252/3/2/006.

[41] Chen, F. F., "Lectures Notes on Langmuir Probe Diagnostics," , 2003. https://doi.org/10.1002/ctpp.201100051.

[42] Chen, F. F., "Langmuir probes in RF plasma: Surprising validity of OML theory," *Plasma Sources Science and Technology*, Vol. 18, No. 3, 2009. https://doi.org/10.1088/0963-0252/18/3/035012.

[43] Chen, F. F., "Langmuir probe analysis for high density plasmas," *Physics of Plasmas*, Vol. 8, No. 6, 2001, pp. 3029–3041. https://doi.org/10.1063/1.1368874.

[44] Lobbia, R. B., and Beal, B. E., "Recommended practice for use of langmuir probes in electric propulsion testing," *Journal of Propulsion and Power*, Vol. 33, No. 3, 2017, pp. 566–581. https://doi.org/10.2514/1.B35531.

[45] Sansonetti, J. E., and Martin, W. C., "Handbook of basic atomic spectroscopic data," *Journal of Physical and Chemical Reference Data*, Vol. 34, No. 4, 2005, pp. 1559–2259. https://doi.org/10.1063/1.1800011.

[46] Woodgate, G. K., *Elementary Atomic Structure*, Oxford University Press, 1980.

[47] Suzuki, M., Katoh, K., and Nishimiya, N., "Saturated absorption spectroscopy of Xe using a GaAs semiconductor laser," *Spectrochimica Acta - Part A Molecular and Biomolecular Spectroscopy*, Vol. 58, No. 11, 2002, pp. 2519–2531. https://doi.org/10.1016/S1386-1425(02)00069-0.

[48] Smith, T., Ngom, B., Linnell, J., and Gallimore, A., "Diode Laser-Induced Fluorescence of Xenon Ion Velocity Distributions," , No. July, 2005, pp. 11–13. https://doi.org/10.2514/6.2005-4406.

[49] Sargsyan, A., Tonoyan, A., Hakhumyan, G., Leroy, C., Pashayan-Leroy, Y., and Sarkisyan, D., "Atomic transitions of Rb, D2 line in strong magnetic fields: Hyperfine Paschen-Back regime," *Optics Communications*, Vol. 334, 2015, pp. 208–213. https://doi.org/10.1016/j.optcom.2014.08.022.

[50] Broström, L., Kastberg, A., Lidberg, J., and Mannervik, S., "Hyperfine-structure measurements in Xe II," *Physical Review A - Atomic, Molecular, and Optical Physics*, Vol. 53, No. 1, 1996, pp. 109–112. https://doi.org/10.1103/PhysRevA.53.109.

[51] Fuller, G. H., "Nuclear Spins and Moments," *Journal of Physical and Chemical Reference Data*, Vol. 5, No. 4, 1976, pp. 835–1092. https://doi.org/10.1063/1.555544.

[52] Kopfermann, H., *Nuclear Moments*, Academic Press, 1958. https://doi.org/10.1016/b978-1-4832-3061-0.50001-5.

[53] Phelps, "database, www.lxcat.net, retrieved on September 27, 2021." , ????

[54] Pullins, S., Chiu, Y. H., Levandiera, D. J., and Dressier, R. A., "Ion dynamics in hall effect and ion thrusters: Xe+ + Xe symmetric charge transfer," *38th Aerospace Sciences Meeting and Exhibit*, 2000. https://doi.org/10.2514/6.2000-603.

[55] Lafleur, T., "Helicon plasma thruster discharge model," *Physics of Plasmas*, Vol. 21, No. 4, 2014. https://doi.org/10.1063/1.4871727, URL http://dx.doi.org/10.1063/1.4871727.